

Theory-Guided Inelastic Neutron Scattering of Crystalline Alkaline Aluminate Salts Bearing Principal Motifs of Solution-State Species

Micah P. Prange,* Trent R. Graham, Rafal Gorniak, Maxime Pouvreau, Mateusz Dembowski, Hsiu-Wen Wang, Luke L. Daemen, Gregory K. Schenter, Mark E. Bowden, Emily T. Nienhuis, Kevin M. Rosso, Aurora E. Clark, and Carolyn I. Pearce



Cite This: *Inorg. Chem.* 2021, 60, 16223–16232



Read Online

ACCESS |



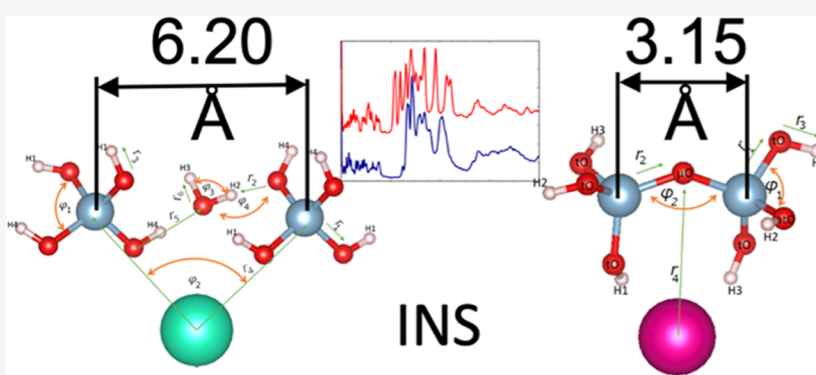
Metrics & More



Article Recommendations



Supporting Information



ABSTRACT: Aluminate salts precipitated from caustic alkaline solutions exhibit a correlation between the anionic speciation and the identity of the alkali cation in the precipitate, with the aluminate ions occurring either in monomeric $\text{Al}(\text{OH})_4^-$ or dimeric $\text{Al}_2\text{O}(\text{OH})_6^{2-}$ forms. The origin of this correlation is poorly understood as are the roles that oligomeric aluminate species play in determining the solution structure, prenucleation clusters, and precipitation pathways. Characterization of aluminate solution speciation with vibrational spectroscopy results in spectra that are difficult to interpret because the ions access a diverse and dynamic configurational space. To investigate the $\text{Al}(\text{OH})_4^-$ and $\text{Al}_2\text{O}(\text{OH})_6^{2-}$ anions within a well-defined crystal lattice, inelastic neutron scattering (INS) and Raman spectroscopic data were collected and simulated by density functional theory for $\text{K}_2[\text{Al}_2\text{O}(\text{OH})_6]$, $\text{Rb}_2[\text{Al}_2\text{O}(\text{OH})_6]$, and $\text{Cs}[\text{Al}(\text{OH})_4] \cdot 2\text{H}_2\text{O}$. These structures capture archetypal solution aluminate species: the first two salts contain dimeric $\text{Al}_2\text{O}(\text{OH})_6^{2-}$ anions, while the third contains the monomeric $\text{Al}(\text{OH})_4^-$ anion. Comparisons were made to the INS and Raman spectra of sodium aluminate solutions frozen in a glassy state. In contrast to solution systems, the crystal lattice of the salts results in well-defined vibrations and associated resolved bands in the INS spectra. The use of a theory-guided analysis of the INS of this solid alkaline aluminate series revealed that differences were related to the nature of the hydrogen-bonding network and showed that INS is a sensitive probe of the degree of completeness and strength of the bond network in hydrogen-bonded materials. Results suggest that the ionic size may explain cation-specific differences in crystallization pathways in alkaline aluminate salts.

1.0. INTRODUCTION

Understanding aluminum (Al) speciation in extremely alkaline solutions remains an important and unique technical challenge. An example application is the retrieval, processing, and vitrification of caustic nuclear waste stored in underground tanks at the Hanford site in Washington State, USA.^{1,2} Solid Al species predominantly exist as aluminum hydroxide (gibbsite) and aluminum oxyhydroxide (boehmite) that reside in contact with radioactive and highly alkaline sodium hydroxide-rich solutions.³ Waste retrieval and processing is beset by uncertainties in Al solubilities that make it difficult to predict how gibbsite and boehmite will evolve in response to dilution or additions, including processes that cause particles to grow (e.g., agglomeration and precipitation of dissolved ions⁴) or

shrink (e.g., dissolution and colloid fragmentation⁵). Studies reveal slow precipitation kinetics and a propensity for supersaturation.^{6,7} Therefore, a robust understanding of Al speciation in solutions and solids under analogous conditions would be beneficial.

In such highly alkaline solutions, the aluminate monomer ($\text{Al}(\text{OH})_4^-$) tends to be the predominant species, shown by

Received: July 2, 2021

Published: October 13, 2021



nuclear magnetic resonance spectroscopy, potentiometry, X-ray diffraction, and optical vibrational spectroscopy.⁸ Although many polymerized Al species have been proposed,⁹ their isolation is difficult due to the temporally and spatially disordered nature of solutions, which limits the sensitivity of spectroscopic and diffraction-based techniques to the relative concentrations of different molecular-scale structural motifs.^{10–12} Nonetheless, vibrational spectroscopy strongly suggests the presence of a μ -oxo-bridged aluminate species $\text{Al}_2\text{O}(\text{OH})_6^{2-}$ (where an oxo ligand bridges the two Al^{3+}) supported by comparisons with crystalline $\text{M}_2[\text{Al}_2\text{O}(\text{OH})_6]$ ($\text{M} = \text{K}^+$ or Rb^+ , see Figures 1 and 2)^{13–15} salt phases containing this dimer, as well as by theoretical simulations.^{16–18}

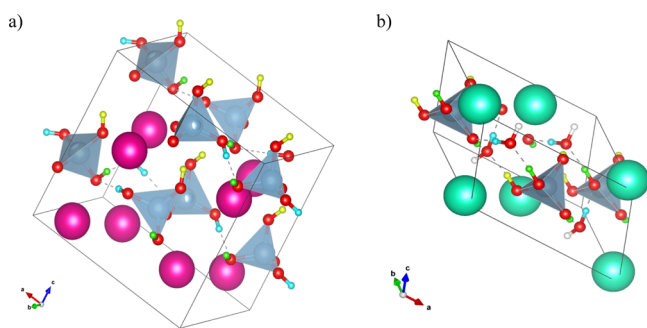


Figure 1. DFT-optimized structures of the (a) orthorhombic μ -oxo dimeric aluminate ($\text{Rb}_2[\text{Al}_2\text{O}(\text{OH})_6]$ or the isostructural $\text{K}_2[\text{Al}_2\text{O}(\text{OH})_6]$) and (b) monoclinic, monomeric aluminate hydrate ($\text{Cs}[\text{Al}(\text{OH})_4] \cdot 2(\text{H}_2\text{O})$). O atoms are displayed in small red spheres, Al tetrahedra in gray, and the alkali metals in large pink (K or Rb) and green (Cs) spheres. The H atoms are color-coded by their orbits under the symmetries of the crystal: H1 (cyan), H2 (green), H3 (yellow), and H4 (white, only in the monoclinic structure). Figure 2, below, shows a different view of the same structures.

Alkaline aluminate salts of this kind have proven to be convenient analogue phases to better understand the molecular principles that organize alkali cations, hydroxide, and water molecules around Al under highly alkaline conditions. For example, both $\text{K}_2[\text{Al}_2\text{O}(\text{OH})_6]$ and $\text{Rb}_2[\text{Al}_2\text{O}(\text{OH})_6]$ can be

easily precipitated for detailed study before, during, and after crystallization. The situation is rather different in concentrated sodium aluminate solutions, which do not yield an equivalent $\text{M}_2[\text{Al}_2\text{O}(\text{OH})_6]$ salt phase, although trace amounts of a $\text{Na}_2[\text{Al}_2\text{O}(\text{OH})_6]$ salt were recently detected in sodium aluminate hydrates.¹⁹ At low total $[\text{NaOH}]$, gibbsite, its structural polymorph bayerite, and boehmite are the solubility-controlling phases, and these minerals have octahedrally coordinated Al in a hydroxy- or oxy-bridged network. However, when total $\text{Na}^+/\text{Al}(\text{OH})_4^-$ ratios are greater than 1 and total $[\text{NaOH}]$ is above ~ 10 m (molality), gibbsite (or bayerite or boehmite) gives way to solubility-controlling phases of (1) monosodium aluminate hydrate ($\text{Na}_2[\text{Al}_2\text{O}_3(\text{OH})_2] \cdot 1.5\text{H}_2\text{O}$) composed of chains of tetrahedral aluminates each coordinated to three bridging oxygens and one terminal hydroxy group and/or (2) nonasodium bis(hexahydroxy aluminate) trihydroxide hexahydrate ($\text{Na}_9[\text{Al}(\text{OH})_6]_2(\text{OH})_3 \cdot 6\text{H}_2\text{O}$), in which aluminum speciates as monomeric aluminate octahedra coordinated to six hydroxides.^{19–24} It is noteworthy that none of the crystalline solids in the sodium case have any significant topological resemblance to the monomeric $\text{Al}(\text{OH})_4^-$ and μ -oxo-bridged dimeric $\text{Al}_2\text{O}(\text{OH})_6^{2-}$ speciation in solution.²⁵

The present study aims to advance understanding of the cation-specific differences in the crystallized aluminate motif through comparison of solid-state vibrational spectra with ab initio calculations based on density functional theory (DFT). We focus on prediction of measured inelastic neutron scattering (INS) spectra for various compounds, which is sensitive to their structural OH- and H-bonding interactions, complemented by Raman spectroscopy. In addition to $\text{K}_2[\text{Al}_2\text{O}(\text{OH})_6]$ and $\text{Rb}_2[\text{Al}_2\text{O}(\text{OH})_6]$, we also examine the monomeric aluminate salt $\text{Cs}[\text{Al}(\text{OH})_4] \cdot 2\text{H}_2\text{O}$ (Figure 1b), together comprising a series that was recently investigated using vibrational (Raman and infrared), X-ray absorption, and nuclear magnetic resonance spectroscopy.²⁶ However, INS is much more sensitive to the locations and dynamics of the protons in the structure, so the present study strongly complements this prior work. INS furthermore uniquely accesses vibrational modes forbidden by the selection rules

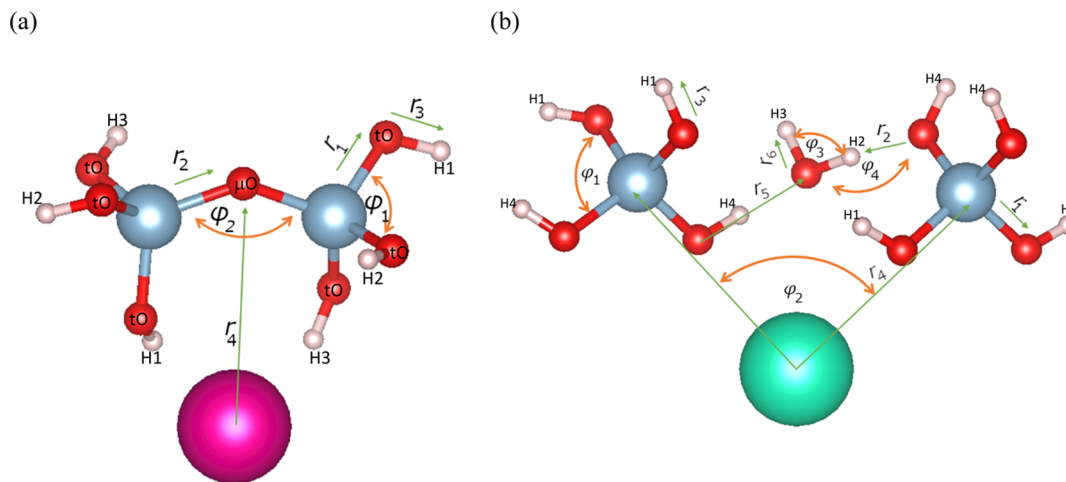


Figure 2. Local environment of the (a) μ -oxo dimer motif in K- and Rb-aluminate salts and the (b) aluminate monomer motif and water molecule in Cs-aluminate hydrate. O atoms are displayed in red, Al atoms are displayed in gray, and the alkali metals are displayed in pink (K and Rb) and green (Cs). Some bond distances and angles are labeled; the corresponding values can be found in Table 3.

governing Raman spectroscopy, making their comparison highly synergistic.

The crystalline salts shown in Figure 1 possess sharp, well-resolved peaks in INS spectra. DFT simulations enable these peaks to be assigned to various vibrational modes of H-containing constituents (aluminate monomer and dimer and water) and the hydrogen-bond network that links them. The librational dynamics (rotational oscillations) are particularly sensitive to the local bonding environment and occur on timescales that can be feasibly achieved in computer simulations. Furthermore, the INS spectra of these crystalline prototypical systems are here directly compared to INS data for concentrated sodium aluminate solutions frozen into a glassy state. Analysis of the various measured INS spectra reveals that the librational bandwidth and the number of peaks in the solid-state spectra encompass the range of hydrogen-bonding environments encountered by protons. In particular, the μ -oxo salts contain H sites not involved in hydrogen bonding that contribute low energy-loss peaks to the librational region, whereas the monomeric salt has no such modes. In addition to elucidating key dynamic properties of the H-bonding network that may ultimately be responsible for the metastability of concentrated/supersaturated sodium aluminate solutions, this study shows how theory-guided analysis of INS data is useful for characterizing the distribution of hydrogen-bond strengths and the degree of proton order in hydrogen-bearing materials.

2.0. METHODS

2.1. Synthesis of Crystalline K-, Rb-, and Cs-Aluminate Salts and Sodium Aluminate Solutions. The synthesis of $K_2[Al_2O(OH)_6]$, $Rb_2[Al_2O(OH)_6]$, and $Cs[Al(OH)_4] \cdot 2H_2O$ was performed in a N_2 -filled glovebox, with ambient water concentrations maintained below 1 ppm. The N_2 atmosphere also limits sorption of CO_2 by high pH solutions. The solids were crystallized from concentrated alkali aluminate solutions prepared from the dissolution of Al wire in concentrated alkali hydroxide solutions.^{26,27} The solutions were prepared by dissolution of 62 mmol alkali hydroxide salt [i.e., 3.49 g of KOH (>85%, Fisher Scientific) or 7.47 g of RbOH·H₂O (99.8%, Strem Chemicals) or 10.41 g of CsOH·H₂O (99.5%, Acros Organics)] into a 30 mL fluorinated ethylene polymer beaker. Then, 4.00 g of H₂O (18 MΩ cm) was added. The dissolution of these salts is exothermic. After waiting for 1 h, the solution temperature was approximately 20 °C. Subsequently, Al wire (Sigma-Aldrich, 99.999%) was added in ca. 0.10 g increments slowly over a period of 3 days to dissolve a total of 1.00 g (37 mmol) of Al. The resulting white solid was separated via vacuum filtration and washed with absolute ethanol (Fisher Scientific, ACS grade).

Aqueous sodium aluminate solutions were prepared in an argon-filled glovebox by dissolving Al wire (99.999% grade) in sodium hydroxide solution (50 wt % stock solution, Alfa Aesar) with the addition of deionized water (18 MΩ) as needed to achieve the desired total NaOH and NaAl(OH)₄ concentrations (see Table 1, where the aluminate speciation is considered as purely monomeric for convenience). The Ar environment protects against CO₂ capture, which is known to be significant for concentrated NaOH solutions under ambient conditions. The dissolution of Al wire follows the reaction $xAl_{(s)} + yNaOH_{(aq)} + 3xH_2O_{(aq)} \rightarrow xNaAl(OH)_4_{(aq)} + (y - x)NaOH_{(aq)} + (3x/2)H_{2(g)}$, where the predominate form of Al³⁺ is Al(OH)₄[−]. The variable denoted as $(y - x)$ defines the excess amount of NaOH (i.e., free Na⁺ and OH[−] species) that is not associated with the Al(OH)₄[−] monomer (in a 1:1 ratio of Na⁺ and Al(OH)₄[−]) and is subject to change with the formation of dimer or polynuclear aluminate complexes. We abbreviated the two solutions as 12.0 and 16.7 m Na-aluminate solution, respectively. Please also note that the Na⁺/Al(OH)₄[−] ratios in these two solutions are equivalent and they only differ by the degree of dilution. Additionally, based on the

Table 1. Composition of the Sodium Aluminate Solutions

	Na-aluminate solution	
	12.0 m	16.7 m
speciation (molal)		
y: NaOH (total)	18.035	25.004
x: NaAl(OH) ₄	12.026	16.673
y − x: NaOH (ex)	6.009	8.331
salt (mole)		
Na ⁺	18.035	25.004
Al	12.026	16.673
OH [−]	54.113	75.023
H ₂ O	55.506	55.506
ratio		
Na ⁺ (ex)/Al(OH) ₄ [−]	0.50	0.50
Na ⁺ (tot)/Al(OH) ₄ [−]	1.50	1.50
H ₂ O/Al(OH) ₄ [−]	4.61	3.33
H ₂ O/Na ⁺ (total)	3.08	2.22

existing thermodynamics model,^{19,24,28} the maximum solubility of the sodium aluminate solution system is near 2 m Al_{tot}³⁺ and 10 m Na_{tot}⁺. This means that the two solutions prepared are in supersaturated states with respect to either gibbsite or sodium aluminate hydrated salts (mentioned above).

2.2. INS Measurements. INS spectra were recorded on the VISION spectrometer²⁹ at Spallation Neutron Source, Oak Ridge National Laboratory, Tennessee, United States. VISION is an indirect geometry spectrometer with a wide dynamic range (0–4800 cm^{−1} and 0–600 meV) and high energy resolution (1–2%). The final momentum of the scattered neutron is fixed, whereas the momentum of the incident neutron varies as a function of time during the measurement, and only two fixed trajectories in the $Q - E$ ($Q - \hbar\omega$) space are tracked with two detector banks. The measurements were performed at $T = 5.0 \pm 0.1$ K controlled using a closed-cycle refrigerator. Based on previously reported Raman spectroscopy,^{30,31} we believe that the INS samples reflect similar Al speciation to ambient temperature ones.

Raw data were transformed to the generalized vibrational density of states (VDOS) projected on H atoms, which is related to the dynamic form factor $S(Q, \omega)$ by

$$G(\omega) = \frac{6m_H\omega}{n(\omega, T) + 1} \int_{\text{det}} d^3Q \frac{S(Q, \omega)}{\hbar^2 Q^2} \quad (1)$$

where m_H is the proton mass, $n(\omega, T)$ is the Bose occupation factor for the temperature T , and Q and ω are the momentum transfer and energy loss, respectively. The integral is formally over all scattering angles but practically over the detector. Conservation of energy in the collisions is enforced by the property that $S(Q, \omega) = 0$ away from the two-dimensional kinematically allowed surface in three-dimensional Q -space. Since the crystalline salt samples are powders, we consider orientational averages over all incident beam directions in the crystal frame. Equation 1 reduces the data to be comparable to the theoretical H-projected VDOS

$$G(\omega) \sim \sum_{\lambda, i} \int_{\text{BZ}} \frac{d^3Q}{(2\pi)^3} \delta(\omega - \omega_\lambda(Q)) e_\lambda^i(Q) \cdot (e_\lambda^i(Q))^* \quad (2)$$

Here, λ is a branch index for the phonons, $\omega_\lambda(Q)$ is the energy of the phonon branch λ computed for a periodic model of the physical system, and i runs over the H sites in the unit cell. The three-vector $e_\lambda^i(Q)$ is the part of the eigenvector of the dynamical matrix (with eigenvalue $(\omega_\lambda(Q))^2$) at Q pertaining to atom i . The integral is over the Brillouin zone of the periodic model. Although the magnitude of $G(\omega)$ defined by eqs 1 and 2 has physical meaning, in practice, including this work, the spectra are normalized.

2.3. Raman Spectroscopy. Raman spectra were obtained at room temperature using a spectrometer (Horiba LabRam HR)

Table 2. Lattice Parameters Obtained from DFT Relaxations ($T = 0$), AIMD Simulations ($T = 5$ K), and X-ray Diffraction Measurements ($T = 111$ K)^{26a}

	T (K)	$K_2[Al_2O(OH)_6]$			$Rb_2[Al_2O(OH)_6]$			$Cs[Al(OH)_4] \cdot 2H_2O$			
		a (Å)	b (Å)	c (Å)	a (Å)	b (Å)	c (Å)	a (Å)	b (Å)	c (Å)	b (deg)
expt	111	10.1605 (12)	7.5416 (8)	9.9990 (12)	10.3510 (8)	7.6820 (7)	10.2480 (8)	10.4310 (3)	6.7090 (2)	6.2190 (2)	126.120 (1)
RPBE-D3 ^{35,44}	300	10.20 (0.38%)	7.70 (2.6%)	10.30 (3.9%)	10.470 (1.2%)	7.860 (2.4%)	10.570 (2.4%)	11.100 (6.7%)	6.070 (−9.3%)	6.840 (10%)	127.330 (0.96%)
PBE ³⁶	0	10.226(0.64%)	7.610 (0.91%)	10.200 (2.0%)	10.430 (0.84%)	7.740 (0.76%)	10.490 (2.4%)	10.670 (2.4%)	6.610 (−1.4%)	6.240 (0.78%)	125.600 (−0.41%)
PBE-D3 ³⁵	0	10.090 (−0.62%)	7.560 (0.25%)	10.040 (0.49%)	10.310 (−0.34%)	7.680 (−0.0031%)	10.330 (0.86%)	10.590 (1.53%)	6.490 (−3.24%)	6.250 (0.59%)	125.700 (−0.34%)
PBE0 ³⁷	0	10.150 (−0.098%)	7.550 (0.18%)	10.080 (0.87%)	10.360 (0.16%)	7.680 (0.0024%)	10.360 (1.1%)	10.740 (3.23%)	6.450 (−2.97%)	6.210 (−0.039%)	124.400 (−1.36%)

^aWe also report structural parameters from the AIMD simulations ($T = 300$ K) of ref 26. Experimental uncertainties (for the X-ray diffraction) and fractional disagreement with the experiment (for the theoretical structures) are given in parentheses.

Table 3. Comparison of Selected Internal Structural Parameters from PBE-D3 Relaxations and X-ray Diffraction Measurements^a

compound	structural properties									
	distances (Å)						angles (deg)			
	r_1	r_2	r_3	r_4	r_5	r_6	φ_1	φ_2	φ_3	φ_4
PBE-D3										
$Cs[Al(OH)_4] \cdot 2H_2O$	1.776	1.659	0.994	4.341	2.731	1.013	108.47	83.46	105.8	173.41
$K_2[Al_2O(OH)_6]$	1.799	1.747	0.985	2.821			106.32	132.12		
$Rb_2[Al_2O(OH)_6]$	1.800	1.745	0.987	3.002			105.86	136.34		
exp										
$Cs[Al(OH)_4] \cdot 2H_2O$	1.750 (3)			4.2060 (9)	2.6760 (19)		113.20 (8)	88.0 (3)		
$K_2[Al_2O(OH)_6]$	1.760 (3)	1.770 (3)	0.90 (4)	2.810 (3)			107.90 (13)	133.0 (2)		
$Rb_2[Al_2O(OH)_6]$	1.760 (4)	1.7200 (19)	0.90 (8)	3.060 (3)			108.40 (16)	136.0 (3)		

^aExperimental data for K and Rb salts are from ref 26. See Figure 2 for definitions of the symbols. Numbers in parentheses are experimental uncertainties in the last digit(s).

installed on an inverted microscope (Nikon Ti-E) by the application of a continuous 632.81 nm laser with a 40× objective. The spectrum was acquired between 100–3900 cm^{-1} . A select region spanning between 400–800 cm^{-1} contains diagnostic Raman peaks for aluminate ions, and this region was deconvoluted using a single polynomial to remove the background followed by regression of Lorentzian line shape parameters.

2.4. DFT Calculations. Structural relaxations and vibrational calculations were performed using the VASP code³² and the popular PAW method³³ to soften the Kohn–Sham potential. The calculations employed converged k -point grids ($9 \times 9 \times 9$) and plane-wave bases defined by an energy cutoff of 750 eV for semilocal functionals and 500 eV for the more expensive hybrid PBE0 calculations. The phonon calculations were performed using fully relaxed structures and the frozen phonon method as implemented in the phonopy package. The force constants were determined using finite differences of DFT calculations on structures with a single atom displaced by 0.01 Å along a crystallographic axis in $1 \times 2 \times 1$ or $1 \times 2 \times 2$ supercells for the structures depicted in Figure 1 a and b, respectively. These calculations were performed using the same exchange–correlation functional and basis sets (e.g., PBE and a 750 eV energy cutoff) as the relaxations. Subsequently, the dynamical matrix was found by Fourier transformation and diagonalized to yield the phonon frequencies and eigenvectors. The DFT calculations employed a variety of popular functionals^{34–37} in an attempt to understand the sensitivity of the relaxed structure to the exchange–correlation approximation.

DFT-based molecular dynamics (NVT ensemble, $T = 5$ K) were performed with the CP2K package³⁸ using the PBE functional with the empirical D3 dispersion corrections,³⁹ with a Gaussian and plane-wave (GPW⁴⁰) basis set together with Goedecker–Teter–Hutter pseudopotentials, a plane wave cutoff of 600 Ry, and a double- ζ basis set with a single set of polarization functions (DZVP-MOLOPT⁴¹).

3.0. RESULTS AND DISCUSSION

3.1. Structure of the K-, Rb-, and Cs-Aluminate Salts.

The structures of the dimeric²⁷ and monomeric²⁶ salt crystals, as determined by single-crystal diffraction, have been reported before and can be obtained from the Crystallography Open Database.⁴² The Cs-aluminate hydrate structure,²⁶ however, is incomplete due to the lack of hydrogen positions. Here, the Cs-aluminate salt has been re-examined with single-crystal X-ray diffraction, and a revised experimental structure is being published separately.⁴³ The proton positions were determined by DFT relaxations of the structure. There are three types of H atoms in the structure of dimeric salts (color-coded in Figure 1a and labeled in Figure 2a). The bridging oxygen that is shared by the dimerized tetrahedra is not bonded to any H atoms. The three symmetry-distinct H atoms are covalently bonded to the terminal O atoms (tO), composing the face of the tetrahedron opposite the oxo bridge. H1 and H2 participate in hydrogen bonds with the neighboring aluminate groups, while H3 does not. In the Cs-aluminate hydrate structure, there are four crystallographically distinct hydrogens (color-coded in Figure 1b and labeled in Figure 2b), two are on the structural water (H2 and H3) and two belong to the unique aluminate group. All of the protons in this structure participate in hydrogen-bonding interactions.

Structural relaxations performed with a variety of exchange–correlation approximations are presented in Table 2. We found that PBE-D3, a common generalized gradient approximation augmented with the semiempirical dispersion correction of Grimme,³⁵ predicts lattice parameters closely matching the experimental values (within 1%) for the dimeric salts. The

monomeric salt, however, is not as well represented by many flavors of DFT (including the hybrid PBE0 functional), for example, PBE-D3 underpredicts the b lattice parameter by $\sim 3\%$. In fact, for the exchange–correlation functionals tested, the b lattice parameter in the monomeric salt shows the largest discrepancy to the measured value. Selected bond distances and angles from PBE-D3 relaxations are summarized and compared to the available experimental values in Table 3.

3.2. INS Investigations on the K-, Rb-, and Cs-Aluminate Salts. In hydrogen-containing systems, the large incoherent scattering cross section for H atoms (about 80 times greater than that of other elements in these systems) makes INS ideal to study hydrogen-bonding interactions because all modes involving hydrogen movement are visible. In the energy range studied here, the features in the measured INS spectra (at 5 K) can be divided into three regions that correlate with different molecular level phenomena. (i) The translational region (Figure 3a) consists of a group of low-intensity peaks extending from the elastic peak at 0 to ~ 400 cm^{-1} , arising from the sublattice oscillations commonly seen in hydrogen-bonded crystals. (ii) The librational region (Figure

3b), containing the most prominent features between ~ 500 and ~ 1250 cm^{-1} , is composed of water librational motions (rotational oscillations) and the motions of H atoms that are covalently bonded to the oxygens of aluminate anions (hereafter referred to as aluminate OH ligands). (iii) The higher energy losses are dominated by multiphonon processes and other backgrounds.⁴⁵ In Figure 3, the features in the measured INS spectra have been labeled (black numbers), and putative assignments of the corresponding features in the simulated spectra have been made (corresponding yellow numbers). The simulated INS spectra (Figure 3) are the hydrogen-projected VDOSs from frozen phonon calculations, arbitrarily broadened by a Gaussian point spread function with a full width at half-maximum of 15.7 cm^{-1} (eq 2). This is a theoretical prediction of the contribution to the INS spectrum of single-phonon scattering from H atoms. For clarity, the simulated total (yellow curves) and partial VDOSs (red and blue curves) are vertically scaled by arbitrary factors for each sample plot shown in Figure 3. Simulated INS spectra using DFT-based molecular dynamics (Figure S1) or including overtones (Figure S2) are shown in the Supporting Information.

Overall, there is a fair agreement between the simulated and measured INS spectra. The broad agreement of the simulations, using diverse codes, methods, and DFT approximation schemes, provides a high level of confidence in the interpretation of experimental observations. In Figure 3, the partial VDOS has been decomposed into contributions from different classes of H atoms. For the dimeric salts (Rb- and K-aluminate), the VDOSs of hydrogen-bonded OH ligands (H1 and H2 atoms) are shown in blue, the VDOS of the non-hydrogen-bonded OH ligand (H3 atom) is shown in red, and the summation of both curves is showed in dashed yellow. For the monomeric salt (Cs-aluminate), since all H atoms are involved in hydrogen bonding, the partial VDOS is decomposed into H atoms that belong to either aluminate groups (blue) or water molecules (red). The motion of aluminate OH ligands (in both the dimer and monomer) can be further decomposed into “riding” and “bending” modes, by considering the motion of H as the sum of the motion of the O atom and the relative motion of the O and H. In the energy regions considered here, the relative motion can justifiably be classified as bending because it is completely perpendicular to the covalent O–H bond (O–H bond stretching in the ligand occurs between 2800 and 3700 cm^{-1} in the simulations). This decomposition can be carried out for velocities in molecular dynamics trajectories, or eigenvectors of the dynamical matrix, and does not depend on the point symmetries of individual molecular groups or the space group of the crystal. However, the corresponding INS intensities of the OH ligand riding and bending modes will not sum to the total intensities because these two motions (riding and bending) are not orthogonal to each other. The riding modes of all OH ligands (quantified as the O VDOS) are illustrated with solid yellow curves in Figure 3b. Note that plotting using this normalization amplifies the riding motion by a factor of $m_{\text{O}}/m_{\text{H}} \approx 16$, which suggests that, in the librational region, riding motions make a very small relative contribution.

To aid the mode assignments in the INS data, room temperature Raman spectra were collected at room temperature for the three salts in the range 100–1900 cm^{-1} (Figure 4). This spectral region includes Al–O stretches and aluminate hydroxyl and water bending modes. We note that the structural

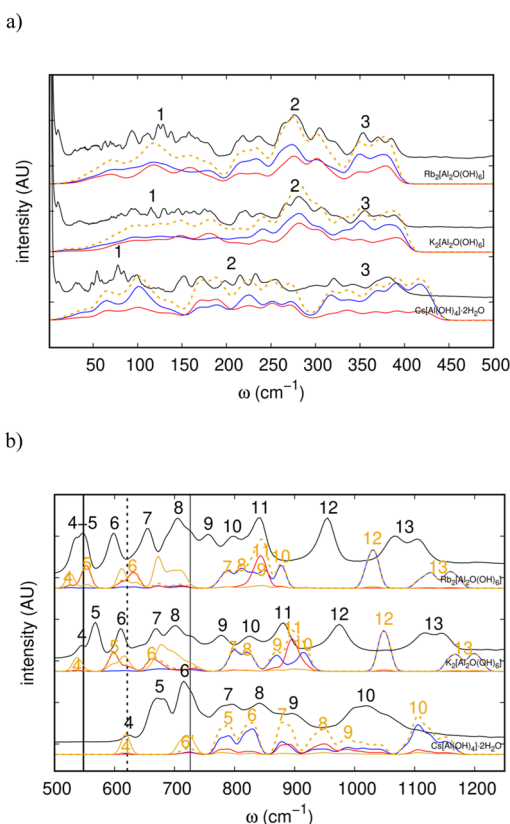


Figure 3. Measured (black) and simulated (dashed yellow) INS spectra of the aluminate-bearing salts in the translational (a) and librational (b) regions. In each panel, the spectra are vertically offset for clarity with Rb-, K-, and Cs-aluminate salts ordered from top to bottom. The red curves denote the contribution from the non-hydrogen-bonded H3 site (in K and Rb salts) or water hydrogens H2 and H3 (in Cs salt), while the blue one is the remainder of the signal. The solid yellow line in panel (b) is the riding motion. Black numerals mark features in the experimental spectra; the yellow numerals mark the corresponding features in the simulated spectra. The vertical solid lines mark the Raman-active bands for the K- and Rb-aluminate salt, and the vertical dashed line mark the Raman-active band for the Cs-aluminate salt.

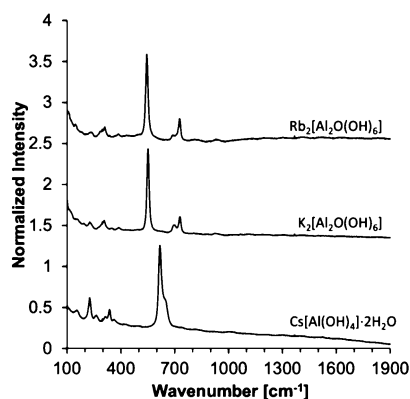


Figure 4. Raman spectra of the three alkaline aluminate salts at room temperature. In each panel, the spectra are vertically offset for clarity.

water molecules in the Cs salt do not contribute any discernible peaks to the Raman spectrum, consistent with previous work.⁴⁶ We could not find any such peaks in the INS, either, although there is interference from multiphonon processes and backgrounds in the relevant spectral region above 1200 cm^{-1} in our experiments. Previous Raman studies have shown that the Al–O bond stretching of aluminate tetrahedra is well resolved for the dimeric (K- and Rb-aluminate salts) versus monomeric (Cs-aluminate salt) structural motifs.²⁶ There are two strongly Raman-active bands for the symmetric Al–O stretching vibrations at ~ 548 and ~ 726 cm^{-1} in the dimeric salts (Figure 4; see also Table S1 for detailed peak assignments). The monomeric salt has only one main peak centered at ~ 621 cm^{-1} for the symmetric Al–O stretching vibrations (Figure 4 and Table S1). These features appear in the INS spectra as minor features with significant OH ligand riding character and are complementary to the OH ligand bending modes that dominate the overall features in the librational spectra, especially at higher frequencies (Figure 3b). In terms of the internal vibrational modes of the aluminate monomer and dimer motifs, the librational bands of the INS spectra contain minor contributions from Al–O stretches and major contributions from aluminate hydroxyl bending modes (i.e., $\nu\text{Al–O}$ and $\delta\text{Al–O–H}$, respectively, in the notation of ref 16). We have summarized all the dominant attributions in terms of the motion of internal coordinates $\nu\text{Al–O}$ and $\delta\text{Al–O–H}$ in Table S2.

The Raman-active modes appear at the highest frequencies in the riding mode bands because the optical transitions occur at $Q = 0$ (i.e., zone center) which corresponds to the maximum of the phonon dispersion curves for such optical modes. INS is sensitive throughout the Brillouin zone, a fact that can be interpreted as freedom from optical selection rules related to the translational symmetry of the crystal. In Figure 3b, these Raman-active bands are marked by vertical solid lines for the K- and Rb-aluminate salt and a vertical dashed line for the Cs-aluminate salt. Even though the Raman data were collected at room temperature, we expect the temperature dependence of the peak locations to be weak and hence comparable to the vibrational frequencies measured by the INS experiments, which were conducted at 5 K.

By comparing the experimental and simulated INS spectra and the corresponding Raman data, the following observations can be made. The translational region lineshapes consist of broad peaks 1–3 (Figure 3a), which are well-reproduced by

DFT calculations, except at low energy loss. Simulations for Cs-aluminate are blue-shifted (~ 25 cm^{-1}) relative to the experimental spectrum, and a smaller blue shift (~ 5 cm^{-1}) is observed for the dimeric salts (Figure 3a). In general, these modes involve motions of all H atoms, although peaks 1 and 3 in the Cs-aluminate salt are dominated by the aluminate groups (blue curve in the bottom spectrum of Figure 3a). In contrast, the peaks in the librational region are dominated by the bending motions of the aluminate OH ligands and are very sensitive to the surrounding hydrogen-bonding environment. For example, in the dimeric salts (Rb- and K-aluminate), peaks 4, 5, 6, and 11 result almost exclusively from excitations of the H3 OH ligand (red curve in the top two spectra in Figure 3b), which does not participate in a hydrogen bond. The appearance of these peaks on the low energy side of the librational band (albeit slightly blue-shifted in the simulation) is a reflection of the smaller restoring force for perturbations of Al–O–H angles compared to Al–O–H \cdots O configuration. Peaks 7–10 and 12–13 are from the H1 and H2 OH ligands, which are involved in hydrogen bonding, that is, Al–O–H \cdots O. This latter set of peaks is significantly blue-shifted in the simulated spectra (blue curve in the top two spectra in Figure 3b). The difference in the theoretical error between these two classes of peaks in the simulated INS spectrum results in the misordering of peaks 10 and 11 in the simulated spectrum. Furthermore, the presence of a non-hydrogen-bonded OH ligand (H3 atom) results in the low-energy librational features (< 600 cm^{-1}) in the dimeric salts. INS studies of other solid aluminate systems with unsaturated hydrogen-bond networks likewise show strong inelastic scattering in this region.⁴⁷ In the monomeric salt, all H atoms participate in hydrogen-bonding interactions, and the start of the librational peaks occurs at higher wavenumbers (above 600 cm^{-1}).

Unlike peaks associated with bending motions of aluminate OH ligands, those associated with the riding motion are slightly red-shifted in the simulation, relative to the experimental spectra (solid yellow curve in Figure 3b). For example, the solid yellow curve for the OH ligand riding motion in the dimeric salts is slightly shifted to the left of the vertical solid lines for the Raman-active Al–O stretching bands. The riding mode near to peak 4 in the Cs-aluminate salt is also in a close agreement with the vertical dashed line for the Raman-active Al–O stretching vibration (Figure 3b). Furthermore, in the Cs-aluminate salt, the peak labeled 6' in the simulated spectrum (the bottom spectrum in Figure 3b), which appears as a shoulder on the high energy-loss side of peak 6 in the experimental INS, occurs ~ 107 cm^{-1} below the main peak 6 (which consists of aluminate OH bending) in the simulated INS. For these three salts, the PBE-D3 theory used exhibits different levels of error for different motions: (i) Al–O bond stretching frequencies (indirectly probed by INS as OH ligand riding motions) are slightly underestimated (< 10 cm^{-1}); (ii) OH ligand bending motions in the absence of a hydrogen bond are overestimated by ~ 50 cm^{-1} ; and (iii) OH ligand bending motions in the presence of a hydrogen bond are overestimated by ~ 100 cm^{-1} .

PBE-D3-based molecular dynamics simulations performed at the experimental temperature ($T = 5$ K) and vibrational analysis of the Hessian of the corresponding relaxed structure for the Cs salt also give results that are consistent with the frozen phonon calculations. A comparison between the methods is shown in Figure S1. Accordingly, the theoretical errors can be assigned to the exchange–correlation approx-

imation and not details of the phonon calculation or basis sets. Nevertheless, the shapes of the individual peaks, arising from the relative dispersion of phonon branches of the same type, are well-reproduced. This allows unambiguous mode assignments, except when peaks of different types overlap.

We note that it is Cs that crystallizes in a hydrated salt, despite having lower solvation energies and faster water exchange rates than lighter alkali metal cations. This suggests that the larger ionic radius of Cs holds the aluminate framework open, allowing enough room for structural water to fit in between aluminate groups and complete the hydrogen-bond network, thereby removing the low-energy librational modes from the phonon spectrum. From this, we conclude that the ionic radius of the alkali cation likely selects the crystal structure that precipitates from alkaline aluminate solutions. The small Na cation results in compact structures with extensively bridged tetrahedral aluminate networks or octahedral aluminates, while the medium-sized K and Rb cations result in slightly more open structures with singly bridged aluminate dimers. The Cs-bearing salt has no bridging oxygens at all and instead has monomeric tetrahedral aluminates spaced by molecular water, a structure that provides more protons per metal and allows for a complete hydrogen-bond network to form.

3.3. INS of the Sodium Aluminate Solution in a Glassy State. INS spectra of concentrated sodium aluminate solutions in a glassy state at 5 K (Figure 5) were also collected.

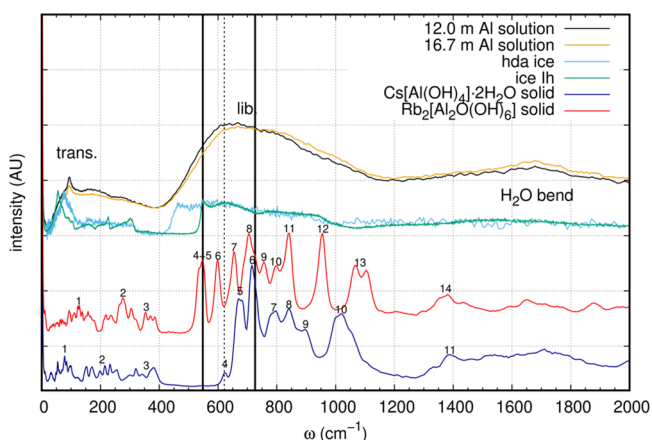
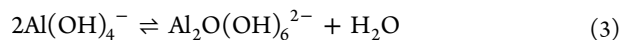


Figure 5. INS spectra of the dilute (black) and concentrated (yellow) Na-aluminate solutions and the Rb-aluminate (red) and Cs-aluminate (blue) salts as collected using VISION. INS spectra of hda ice (light blue) and ice Ih replotted from refs 50–52. Vertical black lines indicate the location of strong Raman transitions associated with monomeric (dashed line) and dimeric (solid lines) aluminate ions in solution. Peak labels on the blue and red INS data are identical to those shown in Figure 3.

At room temperature, these concentrated salt solutions are supersaturated with respect to either monosodium aluminate hydrate ($\text{Na}_2[\text{Al}_2\text{O}_3(\text{OH})_2] \cdot 1.5\text{H}_2\text{O}$) or nonasodium bis-(hexahydroxy aluminate) trihydroxide hexahydrate ($\text{Na}_9[\text{Al}(\text{OH})_6]_2(\text{OH})_3 \cdot 6\text{H}_2\text{O}$) phases.⁴⁸ They are, however, able to remain in the metastable homogeneous liquid state for extended times without precipitation. Upon cooling, and regardless of cooling rate, a glass transition instead of salt crystallization is observed at temperatures below ~ 200 – 150 K, indicating that this concentrated water–salt mixture is a good glass former. The molecular origin of how an aqueous salt

solution can bypass crystallization and vitrify (even if a very slow cooling rate is applied) in these solutions is not well understood, but it is likely correlated to the degree of aluminate oligomerization, as well as the strength of intermolecular interactions between aluminate anions, Na cations, and water molecules. INS investigation of concentrated sodium aluminate solutions can thus provide insights into the strength of intermolecular attraction between aluminate anions and water molecules. To maximize the amount of aluminum-containing species present in solution for interrogation by INS, the solutions studied here were prepared at total aluminum concentrations significantly higher than those found in typical tank wastes.

In the low energy region of the spectra (below 400 cm^{-1}), the broad signal originates from acoustic translational motions of H-bearing species (predominately water molecules, aluminate ions, and hydroxyls). In the librational region (~ 400 up to $\sim 1250\text{ cm}^{-1}$), the observed INS spectra (Figure 5) must be regarded as a superposition of at least two kinds of molecular motions: the libration of (not so free) water molecules and the motion of other H atoms (mostly aluminate OH bending, although $\sim 4\%$ of the intensity is from excess OH^- ions that do not belong to aluminate anions and/or participate in aluminate oligomerization). However, the clear bending librational peaks of the INS spectra for the K-, Rb-, and Cs-aluminate salts (Figure 3) are absent in the sodium aluminate solution spectra due to configurational disorder. Several INS spectra are juxtaposed in Figure 5, including the two vitrified sodium aluminate solutions, the Cs- and Rb-aluminate salts, high-density amorphous (hda) ice, and ordinary ice (ice Ih). Vertical lines indicate the three Raman-active bands assigned to the internal Al–O stretching vibrations, as in Figure 3. The room temperature Raman spectra and the three active bands at energies of ~ 537 , 626 , and 703 cm^{-1} for the two sodium aluminate solutions (Figure S3) are similar to the Raman bands of aluminate salts shown in Figure 4. The ~ 537 and 703 cm^{-1} bands are from the Al–O vibrations in the $\text{Al}_2\text{O}(\text{OH})_6^{2-}$ dimer, and the 626 cm^{-1} band is from the Al–O vibrations in the $\text{Al}(\text{OH})_4^-$ monomer. This reflects the shift in aluminate speciation from the monomer to dimer as the total aluminum concentration increases (see Figure S3 and Table S1).^{12,30} Based on the Lorentzian fits presented in Table S1, we estimate that the monomer–dimer ratio is $\sim 21\%$ higher in the more concentrated solution, assuming that other species do not result in contributions overlapping with these bands, which is the working hypothesis.³⁰ We did not attempt to quantify the activity of the different aluminate solution species or water molecules in the samples. This is to be expected, given that dimer formation, according to eq 3, releases water, and the reduced activity of water in the more concentrated solution would drive the equilibrium in this direction.⁴⁹



Based on estimates from the nominal concentrations (Table 1), water librational motions are responsible for more than 60% of the intensity of the spectra for the Na-aluminate solutions, even at the high salt concentrations studied here (Figure 5). Ice Ih forms a regular hexagonal lattice, but the positions of the H atoms are disordered.⁵⁰ Hda ice has a denser structure produced at high pressure⁵¹ and exhibits a lower onset of the librational region than ice Ih (~ 411 vs $\sim 508\text{ cm}^{-1}$).⁵³ This difference is attributed to a weakening of the

average restoring force for bending motions⁵¹ and follows the same pattern observed in the aluminate salts: the more open structure with greater O–O distances exhibits a higher frequency onset of librational motions of H atoms. The broad librational band in the aluminate solution INS data also has a low-energy librational band onset near 400 cm^{−1}, far below the lowest energy mode contributing to the internal aluminate monomer and dimer vibrations and the bending modes observed in the aluminate salts. Previous work^{54–56} has established that the effect of salt addition is similar to the effect of increasing pressure on the water tetrahedral network: both reduce second shell O–O distances. We conclude that hydrogen-bonded aluminate OH groups contribute to the librational region of the INS spectrum primary above ~640 cm^{−1}. The spectral weight below this frequency is attributed to interaction among the solute waters and non-hydrogen-bonded aluminate hydroxyls. On this basis, the INS spectra show trends in the completeness of the hydrogen-bond network in concentrated water–salt mixtures: changes in the strength of the low energy (below ~640 cm^{−1}) portion of the broad feature in the medium frequency range reflect similar changes in the proportion of aluminate OH groups that do not donate a hydrogen bond.

In the INS spectra, increasing the aluminate concentration shifts spectral weight from the low-energy region to higher frequencies, while the Raman analysis (summarized in Table S2 and Figure S3) indicates that the ratio of aluminate dimers to monomers increases. Thus, taken together, the data suggest that as Al clustering and oligomerization proceed with increasing Al³⁺ concentration, a greater proportion of H sites are included in the hydrogen-bond network that links the various aluminate species to themselves and to the solute. We hypothesize that this strengthening of the hydrogen-bond network, reflected in an increase in the restoring forces for aluminate OH bends, is related to the strong tendency for sodium aluminate solutions to form glasses instead of crystalline phases by providing a free-energy barrier to the structural reorganization needed to crystallize.

4.0. CONCLUSIONS

The INS spectra of crystalline K, Rb, and Cs tetrahedrally coordinated aluminate salts containing monomer and dimer motifs, as well as a Na-aluminate aqueous solution frozen into a glassy state, were measured and, where possible, simulated using DFT. The simulations usefully reproduced the shapes of individual features in these systems. The difference between experimental and predicted vibrational frequencies was correlated to the bonding environment of the contributing H atom and to the type of motion involving the mode. The vibrational frequencies for riding motions had small differences between experimental and predicted values, and the differences between experimental and predicted frequencies of relative motions were larger for H atoms in hydrogen bonds than “free” H atoms.

The librational region in the INS spectrum is a spectroscopic signature that can be used to differentiate between (i) structures and solutions with more water, in which not all H atoms participate in hydrogen bonds, and (ii) structures and solutions with less water, in which the hydrogen-bond network is complete. A broader, more featureful librational region reflects the distribution of frequencies for the OH bending motion and corresponds to an increase in the restoring forces. Thus, INS represents a unique probe of the completeness and

the strength of hydrogen-bond networks. This is demonstrated in the change in the librational region for Na-aluminate aqueous solutions as the amount of water in these concentrated water–salt mixtures decreases. For the crystalline aluminate salts, the presence of structural water in the hydrous Cs monomer salt qualitatively changes the INS spectrum by saturating the hydrogen-bond network.

We conclude that, in alkaline aluminate salts, the alkali cation ionic radius controls the amount of space available to accommodate a hydrogen-bond network and influences the structures formed as they crystallize. In concentrated sodium aluminate solutions, the strength and completeness of the hydrogen-bond network provide a free-energy barrier to the structural reorganization necessary for crystallization; this manifests in a strong tendency to form glasses instead of crystalline phases. The new knowledge provided by this collective experimental and computational INS investigation will inform the behavior of concentrated electrolytes in many energy-related applications such as industrial-scale material processing (including retrieval, processing, and vitrification of caustic nuclear waste), energy-storage systems, and catalysis.

■ ASSOCIATED CONTENT

Supporting Information

The Supporting Information is available free of charge at <https://pubs.acs.org/doi/10.1021/acs.inorgchem.1c02006>.

Comparisons of static and dynamic DFT simulations of the phonons in the aluminate salts; simulations of the INS of the aluminate salts including overtones plotted with the experimental INS and Raman data; assignments of the vibrational modes of the aluminate salts; and decomposition of the solution-phase Raman measurements into individual peaks (PDF)

■ AUTHOR INFORMATION

Corresponding Author

Micah P. Prange – Physical Sciences Division, Physical and Computational Sciences Directorate, Pacific Northwest National Laboratory, Richland, Washington 99352, United States; orcid.org/0000-0002-0775-2024; Email: micah.prange@pnnl.gov

Authors

Trent R. Graham – Physical Sciences Division, Physical and Computational Sciences Directorate, Pacific Northwest National Laboratory, Richland, Washington 99352, United States; orcid.org/0000-0001-8907-8004

Rafal Gorniak – Department of Chemistry, Washington State University, Pullman, Washington 99164, United States

Maxime Pouvreau – Department of Chemistry, Washington State University, Pullman, Washington 99164, United States; orcid.org/0000-0002-9015-5086

Mateusz Dembowski – Physical Sciences Division, Physical and Computational Sciences Directorate, Pacific Northwest National Laboratory, Richland, Washington 99352, United States; orcid.org/0000-0002-6665-8417

Hsiu-Wen Wang – Chemical Sciences Division, Oak Ridge National Laboratory, Oak Ridge, Tennessee 37831, United States; orcid.org/0000-0002-2802-4122

Luke L. Daemen – Neutron Scattering Division, Oak Ridge National Laboratory, Oak Ridge, Tennessee 37831, United States

Gregory K. Schenter – Physical Sciences Division, Physical and Computational Sciences Directorate, Pacific Northwest National Laboratory, Richland, Washington 99352, United States; Department of Chemistry, Washington State University, Pullman, Washington 99164, United States

Mark E. Bowden – Physical Sciences Division, Physical and Computational Sciences Directorate, Pacific Northwest National Laboratory, Richland, Washington 99352, United States; orcid.org/0000-0003-3812-3340

Emily T. Nienhuis – Physical Sciences Division, Physical and Computational Sciences Directorate, Pacific Northwest National Laboratory, Richland, Washington 99352, United States

Kevin M. Rosso – Physical Sciences Division, Physical and Computational Sciences Directorate, Pacific Northwest National Laboratory, Richland, Washington 99352, United States; orcid.org/0000-0002-8474-7720

Aurora E. Clark – Department of Chemistry, Washington State University, Pullman, Washington 99164, United States; Physical Sciences Division, Physical and Computational Sciences Directorate, Pacific Northwest National Laboratory, Richland, Washington 99352, United States; orcid.org/0000-0001-9381-721X

Carolyn I. Pearce – Environmental Subsystem Science Division, Energy and Environment Directorate, Pacific Northwest National Laboratory, Richland, Washington 99352, United States; Department of Crop and Soil Sciences, Washington State University, Pullman, Washington 99164, United States; orcid.org/0000-0003-3098-1615

Complete contact information is available at:

<https://pubs.acs.org/10.1021/acs.inorgchem.1c02006>

Notes

The authors declare no competing financial interest.

ACKNOWLEDGMENTS

This research was supported by IDREAM (Interfacial Dynamics in Radioactive Environments and Materials), an Energy Frontier Research Center funded by the U.S. Department of Energy (DOE), Office of Science, Basic Energy Sciences (BES). PNNL is a multiprogram national laboratory operated for DOE by Battelle Memorial Institute under Contract DE-AC05-76RL0-1830. INS was performed at ORNL's Spallation Neutron Source, supported by the Scientific User Facilities Division, Office of Basic Energy Sciences, US DOE, under contract no. DE-AC0500OR22725 with UT Battelle, LLC. Raman spectroscopy was performed using facilities at the Environmental Molecular Science Laboratory (EMSL, grid.436923.9), a DOE Office of Science User Facility sponsored by the Office of Biological and Environmental Research at Pacific Northwest National Laboratory (PNNL). PNNL is a multiprogram national laboratory operated for DOE by Battelle Memorial Institute under Contract DE-AC05-76RL0-1830.

REFERENCES

- (1) Peterson, R. A.; Buck, E. C.; Chun, J.; Daniel, R. C.; Herting, D. L.; Ilton, E. S.; Lumetta, G. J.; Clark, S. B. Review of the Scientific Understanding of Radioactive Waste at the U.S. DOE Hanford Site. *Environ. Sci. Technol.* **2018**, *52*, 381–396.
- (2) Herting, D. L.; Reynolds, J. G.; Barton, W. B. Conversion of Coarse Gibbsite Remaining in Hanford Nuclear Waste Tank Heels to

Solid Sodium Aluminate [$\text{NaAl}(\text{OH})_4 \cdot 1.5\text{H}_2\text{O}$]. *Ind. Eng. Chem. Res.* **2014**, *53*, 13833–13842.

- (3) Peterson, R. A.; Lumetta, G. J.; Rapko, B. M.; Poloski, A. P. Modeling of Boehmite Leaching from Actual Hanford High-Level Waste Samples. *Sep. Sci. Technol.* **2007**, *42*, 1719–1730.

- (4) Anovitz, L. M.; Zhang, X.; Soltis, J.; Nakouzi, E.; Krzysko, A. J.; Chun, J.; Schenter, G. K.; Graham, T. R.; Rosso, K. M.; De Yoreo, J. J.; Stack, A. G.; Bleuel, M.; Gagnon, C.; Mildner, D. F. R.; Ilavsky, J.; Kuzmenko, I. Effects of Ionic Strength, Salt, and pH on Aggregation of Boehmite Nanocrystals: Tumbler Small-Angle Neutron and X-ray Scattering and Imaging Analysis. *Langmuir* **2018**, *34*, 15839.

- (5) Graham, T. R.; Dembowski, M.; Martinez-Baez, E.; Zhang, X.; Jaegers, N. R.; Hu, J.; Gruszkiewicz, M. S.; Wang, H.-W.; Stack, A. G.; Bowden, M. E.; Delegard, C. H.; Schenter, G. K.; Clark, A. E.; Clark, S. B.; Felmy, A. R.; Rosso, K. M.; Pearce, C. I. In Situ ^{27}Al NMR Spectroscopy of Aluminate in Sodium Hydroxide Solutions above and below Saturation with Respect to Gibbsite. *Inorg. Chem.* **2018**, *57*, 11864–11873.

- (6) Reynolds, J. G.; McCoskey, J. K.; Herting, D. L. Gibbsite Solubility in Hanford Nuclear Waste Approached from above and below Saturation. *Ind. Eng. Chem. Res.* **2016**, *55*, 5465–5473.

- (7) Reynolds, J. G. The apparent solubility of aluminum (III) in Hanford high-level waste. *J. Environ. Sci. Health, Part A: Environ. Sci. Eng.* **2012**, *47*, 2213–2218.

- (8) Sipos, P. The structure of $\text{Al}(\text{III})$ in strongly alkaline aluminate solutions — A review. *J. Mol. Liq.* **2009**, *146*, 1–14.

- (9) Gale, J. D.; Rohl, A. L.; Watling, H. R.; Parkinson, G. M. Theoretical Investigation of the Nature of Aluminum-Containing Species Present in Alkaline Solution. *J. Phys. Chem. B* **1998**, *102*, 10372–10382.

- (10) Radnai, T.; May, P. M.; Hefter, G. T.; Sipos, P. Structure of Aqueous Sodium Aluminate Solutions: A Solution X-ray Diffraction Study. *J. Phys. Chem. A* **1998**, *102*, 7841–7850.

- (11) Sipos, P.; Hefter, G.; May, P. M. ^{27}Al NMR and Raman Spectroscopic Studies of Alkaline Aluminate Solutions With Extremely High Caustic Content — Does the Octahedral Species $\text{Al}(\text{OH})_6^{3-}$ Exist in Solution? *Talanta* **2006**, *70*, 761–765.

- (12) Sipos, P. I.; Schibeci, M.; Peintler, G. b.; May, P. M.; Hefter, G. Chemical Speciation in Concentrated Alkaline Aluminate Solutions in Sodium, Potassium and Caesium Media. Interpretation of the Unusual Variations of the Observed Hydroxide Activity. *Dalton Trans.* **2006**, *15*, 1858–1866.

- (13) Moolenaar, R. J.; Evans, J. C.; McKee, L. D. Structure of the Aluminate Ion in Solutions at High pH. *J. Phys. Chem.* **1970**, *74*, 3629–3636.

- (14) Johnston, C. T.; Agnew, S. F.; Schoonover, J. R.; Kenney, J. W.; Page, B.; Osborn, J.; Corbin, R. Raman Study of Aluminum Speciation in Simulated Alkaline Nuclear Waste. *Environ. Sci. Technol.* **2002**, *36*, 2451–2458.

- (15) Schoonover, J. R.; Zhang, S. L.; Johnston, C. T. Raman Spectroscopy and Multivariate Curve Resolution of Concentrated Al_2O_3 – Na_2O – H_2O Solutions. *J. Raman Spectrosc.* **2003**, *34*, 404–412.

- (16) Pouvreau, M.; Dembowski, M.; Clark, S. B.; Reynolds, J. G.; Rosso, K. M.; Schenter, G. K.; Pearce, C. I.; Clark, A. E. Ab Initio Molecular Dynamics Reveal Spectroscopic Siblings and Ion Pairing as New Challenges for Elucidating Prenucleation Aluminum Speciation. *J. Phys. Chem. B* **2018**, *122*, 7394–7402.

- (17) Guo, J.; Wang, Z.; Cao, J.; Gong, X. Structures of Solvated Tetramethylammonium Aluminate Species and its Transformation Mechanism by DFT and Raman Spectra. *J. Mol. Struct.* **2020**, *1199*, 126791.

- (18) Guo, J.; Liu, S.; Wang, Z.; Cao, J.; Wang, D. Polymerization of Aluminate Monomer in its Initial Nucleation Stage of Organic Alkali Solution Revealed by ReaxFF Molecular Dynamics Simulation. *Chem. Phys. Lett.* **2020**, *739*, 136979.

- (19) Graham, T. R.; Dembowski, M.; Hu, J. Z.; Jaegers, N. R.; Zhang, X.; Clark, S. B.; Pearce, C. I.; Rosso, K. M. Intermediate

Species in the Crystallization of Sodium Aluminate Hydroxy Hydrates. *J. Phys. Chem. C* **2020**, 124, 12337–12345.

(20) Gessner, W.; Weinberger, M.; Müller, D.; Ni, L. P.; Chalajapina, O. B. Zur Kenntnis der kristallinen Phasen in den Systemen $\text{MOAl}_2\text{O}_3\text{H}_2\text{O}$ ($\text{M} = \text{K}, \text{Na}$). *Z. Anorg. Allg. Chem.* **1987**, 547, 27–44.

(21) Weinberger, M.; Schneider, M.; Geßner, W. H.; Müller, D. Die Kristallstruktur des Natriumoxohydroxoaluminathydrates $\text{Na}_2[\text{Al}_2\text{O}_3(\text{OH})_2] \cdot 1.5 \text{ H}_2\text{O}$. *Z. Anorg. Allg. Chem.* **1995**, 621, 679–684.

(22) Weinberger, M.; Schneider, M.; Zabel, V.; Müller, D.; Geßner, W. Nonanatrium-bis(hexahydroxoaluminat)-trihydroxid-hexahydrat ($\text{Na}_9[\text{Al}(\text{OH})_6]_2(\text{OH})_3 \cdot 6\text{H}_2\text{O}$) – Kristallstruktur, NMR-Spektroskopie und thermisches Verhalten. *Z. Anorg. Allg. Chem.* **1996**, 622, 1799–1805.

(23) Zabel, V.; Schneider, M.; Weinberger, M.; Gessner, W. Nonasodium Bis(hexahydroxoaluminate) Trihydroxide Hexahydrate. *Acta Crystallogr., Sect. C: Struct. Chem.* **1996**, 52, 747–749.

(24) Graham, T. R.; Gorniak, R.; Dembowski, M.; Zhang, X.; Clark, S. B.; Pearce, C. I.; Clark, A. E.; Rosso, K. M. Solid-State Recrystallization Pathways of Sodium Aluminate Hydroxy Hydrates. *Inorg. Chem.* **2020**, 59, 6857–6865.

(25) Watling, H. R.; Sipos, P. M.; Byrne, L.; Hefter, G. T.; May, P. M. Raman, IR, and 27 Al-MAS-NMR Spectroscopic Studies of Sodium (Hydroxy)aluminates. *Appl. Spectrosc.* **1999**, 53, 415–422.

(26) Dembowski, M.; Prange, M. P.; Pouvreau, M.; Graham, T. R.; Bowden, M. E.; N'Diaye, A.; Schenter, G. K.; Clark, S. B.; Clark, A. E.; Rosso, K. M.; Pearce, C. I. Inference of principal species in caustic aluminate solutions through solid-state spectroscopic characterization. *Dalton Trans.* **2020**, 49, 5869–5880.

(27) Johansson, G.; Hope, H.; Nevald, R.; Frank, V.; Brunvoll, J.; Bunnenberg, E.; Djerassi, C.; Records, R. The Crystal Structure of the Potassium Aluminate $\text{K}_2[\text{Al}_2\text{O}(\text{OH})_6]$. *Acta Chem. Scand.* **1966**, 20, 505.

(28) Rotmanov, K. V.; Smirnov, M. N. Physicochemical Properties of Aluminate Solutions. *Moscow Univ. Chem. Bull.* **2021**, 76, 85–94.

(29) <https://neutrons.ornl.gov/vision> (accessed May 7, 2021).

(30) Sipos, P.; May, P. M.; Hefter, G. Quantitative Determination of an Aluminate Dimer in Concentrated Alkaline Aluminate Solutions by Raman Spectroscopy. *Dalton Trans.* **2006**, 368–375.

(31) Liu, W.; Yin, Z.-L.; Ding, Z.-y. Low-temperature Phase Transitions of Sodium Aluminate Solutions. *Trans. Nonferrous Met. Soc. China* **2019**, 29, 194–199.

(32) Kresse, G.; Furthmüller, J. Efficient Iterative Schemes For Ab Initio Total-Energy Calculations Using a Plane-Wave Basis Set. *Phys. Rev. B: Condens. Matter Mater. Phys.* **1996**, 54, 11169–11186.

(33) Kresse, G.; Joubert, D. From Ultrasoft Pseudopotentials to the Projector Augmented-Wave Method. *Phys. Rev. B: Condens. Matter Mater. Phys.* **1999**, 59, 1758–1775.

(34) Hammer, B.; Hansen, L. B.; Nørskov, J. K. Improved Adsorption Energetics Within Density-Functional Theory Using Revised Perdew-Burke-Ernzerhof Functionals. *Phys. Rev. B: Condens. Matter Mater. Phys.* **1999**, 59, 7413–7421.

(35) Grimme, S.; Ehrlich, S.; Goerigk, L. Effect of the Damping Function in Dispersion Corrected Density Functional Theory. *J. Comput. Chem.* **2011**, 32, 1456–1465.

(36) Perdew, J. P.; Burke, K.; Ernzerhof, M. Generalized Gradient Approximation Made Simple. *Phys. Rev. Lett.* **1996**, 77, 3865–3868.

(37) Perdew, J. P.; Ernzerhof, M.; Burke, K. Rationale for Mixing Exact Exchange With Density Functional Approximations. *J. Chem. Phys.* **1996**, 105, 9982–9985.

(38) Hutter, J.; Iannuzzi, M.; Schiffrmann, F.; VandeVondele, J. cp2k: atomistic simulations of condensed matter systems. *Wiley Interdiscip. Rev. Comput. Mol. Sci.* **2014**, 4, 15–25.

(39) Grimme, S.; Antony, J.; Ehrlich, S.; Krieg, H. A consistent and accurate ab initio parametrization of density functional dispersion correction (DFT-D) for the 94 elements H-Pu. *J. Chem. Phys.* **2010**, 132, 154104.

(40) VandeVondele, J.; Krack, M.; Mohamed, F.; Parrinello, M.; Chassaing, T.; Hutter, J. Quickstep: Fast and accurate density

functional calculations using a mixed Gaussian and plane waves approach. *Comput. Phys. Commun.* **2005**, 167, 103–128.

(41) VandeVondele, J.; Hutter, J. Gaussian basis sets for accurate calculations on molecular systems in gas and condensed phases. *J. Chem. Phys.* **2007**, 127, 114105.

(42) Gražulis, S.; Chateigner, D.; Downs, R. T.; Yokochi, A. F.; Quirós, M.; Lutterotti, L.; Manakova, E.; Butkus, J.; Moeck, P.; Le Bail, A. Crystallography Open Database—an Open-Access Collection of Crystal Structures. *J. Appl. Crystallogr.* **2009**, 42, 726–729.

(43) Prange, M. P.; Bowden, M. E.; Dembowski, M., The Structure of $\text{Cs}[\text{Al}(\text{OH})_4] \cdot 2\text{H}_2\text{O}$. In prep.

(44) Hammer, B.; Hansen, L. B.; Nørskov, J. K. Improved Adsorption Energetics Within Density-Functional Theory Using Revised Perdew-Burke-Ernzerhof Functionals. *Phys. Rev. B: Condens. Matter Mater. Phys.* **1999**, 59, 7413–7421.

(45) Liu, T.; Gautam, S. S.; Daemen, L. L.; Kolesnikov, A. I.; Anovitz, L. M.; Hartl, M.; Cole, D. R. Vibrational Behavior of Water Adsorbed on Forsterite (Mg_2SiO_4) Surfaces. *ACS Earth Space Chem.* **2020**, 4, 1050.

(46) Wu, L.; Evans, S. F.; Cheng, Y.; Navrotsky, A.; Moyer, B. A.; Harrison, S.; Paranthaman, M. P. Neutron Spectroscopic and Thermochemical Characterization of Lithium–Aluminum-Layered Double Hydroxide Chloride: Implications for Lithium Recovery. *J. Phys. Chem. C* **2019**, 123, 20723–20729.

(47) VandeVondele, J.; Krack, M.; Mohamed, F.; Parrinello, M.; Chassaing, T.; Hutter, J. Quickstep: Fast and a Mixed Gaussian and Plane Waves Approach. *Comput. Phys. Commun.* **2005**, 167, 103–128.

(48) <http://www.cp2k.org> (Nov 18, 2019).

(49) Qiu, G.; Chen, N. Phase Study of the System $\text{Na}_2\text{O}-\text{Al}_2\text{O}_3-\text{H}_2\text{O}$. *Can. Metall. Q.* **1997**, 36, 111–114.

(50) Dembowski, M.; Graham, T. R.; Reynolds, J. G.; Clark, S. B.; Rosso, K. M.; Pearce, C. I. Influence of Soluble Oligomeric Aluminum on Precipitation in the $\text{Al}-\text{KOH}-\text{H}_2\text{O}$ System. *Phys. Chem. Chem. Phys.* **2020**, 22, 24677–24685.

(51) Li, J. Inelastic Neutron Scattering Studies of Hydrogen Bonding in Ices. *J. Chem. Phys.* **1996**, 105, 6733–6755.

(52) Kolesnikov, A. I.; Li, J.; Parker, S. F.; Eccleston, R. S.; Loong, C.-K. Vibrational Dynamics of Amorphous Ice. *Phys. Rev. B: Condens. Matter Mater. Phys.* **1999**, 59, 3569–3578.

(53) Li, J.; Kolesnikov, A. I. Neutron Spectroscopic Investigation of Dynamics of Water Ice. *J. Mol. Liq.* **2002**, 100, 1–39.

(54) Kolesnikov, A. I.; Sinitsyn, V. V.; Ponyatovsky, E. G.; Natkaniec, I.; Smirnov, L. S.; Li, J.-C. Neutron-Scattering Studies of Ice Prepared by Different Thermobaric Treatments. *J. Phys. Chem. B* **1997**, 101, 6082–6086.

(55) Botti, A.; Bruni, F.; Imberti, S.; Ricci, M. A.; Soper, A. K. Ions in Water: The Microscopic Structure of Concentrated NaOH Solutions. *J. Chem. Phys.* **2004**, 120, 10154–10162.

(56) Imberti, S.; Botti, A.; Bruni, F.; Cappa, G.; Ricci, M. A.; Soper, A. K. Ions in Water: The Microscopic Structure of Concentrated Hydroxide Solutions. *J. Chem. Phys.* **2005**, 122, 194509.